Extent of frustration in the classical Kitaev-Γ model via bond anisotropy

Ahmed Rayyan [1], Qiang Luo [1], and Hae-Young Kee [1,2,*]

[1]*Department of Physics and Center for Quantum Materials, University of Toronto, 60 St. George St., Toronto, Ontario M5S 1A7, Canada*

[2]*Canadian Institute for Advanced Research, Toronto, Ontario M5G 1Z8, Canada*

(Received 11 June 2021; revised 31 August 2021; accepted 13 September 2021; published 27 September 2021)

In the pseudospin-$\frac{1}{2}$ honeycomb Mott insulators with strong spin-orbit coupling, there are two types of bond-dependent exchange interactions, named Kitaev (K) and Γ, leading to strong frustration. While the ground state of the Kitaev model is a quantum spin liquid with fractionalized excitations, the ground state of the Γ model remains controversial. In particular, the phase diagram of the $K\Gamma$ model with ferromagnetic K and antiferromagnetic Γ interactions has been intensively studied because of its relevance to candidate materials such as α-$RuCl_3$. Numerical studies also included the effects of tuning the bond strengths, i.e., z-bond strength different from the other bonds. However, no clear consensus on the overall phase diagram has been reached yet. Here we study the classical $K\Gamma$ model with anisotropic bond strengths using Monte Carlo simulations to understand the phases that emerge out of competition between the two frustrated limits. We also address how the anisotropic bond strength affects the phase diagram and strength of quantum fluctuations. We found various large unit cell phases due to the competing frustrations, and analyzed their intrinsic degeneracy based on the symmetry of the Hamiltonian. Using the linear spin wave theory we showed that the anisotropic bond strength enhances quantum fluctuations in the Γ-dominant regime where a small reduced moment is observed. The implications of our findings in relation to the quantum model are also discussed.

DOI: 10.1103/PhysRevB.104.094431

I. INTRODUCTION

The Kitaev spin model on the two-dimensional honeycomb lattice serves as a fascinating example of a quantum spin liquid (QSL) [1]. In particular, the braiding statistics of fractionalized Majorana excitations in the Kitaev spin liquid (KSL) has generated intense interest in both condensed matter physics and quantum information communities due to their application in fault-tolerant quantum computation [2]. A key ingredient of the model is a particular type of bond-dependent interactions resulting in spin frustration, different from more traditional approaches based on geometrical constraints or going beyond nearest-neighbor interactions on bipartite lattices [3–6]. This intriguing model had been a pure theoretical interest until the Jackeli-Khaliullin mechanism [7,8] outlined how the Kitaev interactions are generated in the low-energy description of pseudospin $J_{\text{eff}} = 1/2$ moments in spin-orbit coupled Mott insulators. However, it was shown that in solid-state materials non-Kitaev interactions are inevitable, and a nearest-neighbor generic model includes another bond-dependent off-diagonal exchange term named the Γ interaction in addition to a conventional Heisenberg (J) term [9]. The generic model was studied using a 24-site exact diagonalization (ED), which showed a rich phase diagram including various ordered and disordered phases, but the nature of the disordered phases near the Γ region was not identified [9].

A considerable amount of theoretical effort has been made to pin down the phase diagram of the extended model and to identify the potential QSL in Kitaev candidate materials such as α-$RuCl_3$ [10–24]. While the KSL and various ordered phases are uncovered, there still remains regions of the phase space which are not well understood, with the most peculiar region being that of ferromagnetic (FM) Kitaev and antiferromagnetic (AFM) Γ interactions ($K\Gamma$ model). Several numerical simulations of the $K\Gamma$ model have reported quantum-disordered phases [25–32], but the phase diagram is still controversial [33]. The classical $K\Gamma$ model in a small phase space near the pure Kitaev [34–39] or pure Γ region was also studied [19,30,40–43]. They revealed the macroscopic degeneracy at the pure Kitaev and Γ limits [44,45], and the large unit cells (LUCs) that cannot be captured by small clusters used in, for example, ED on the 24-site cluster.

These studies have focused on the isotropic limit, where the exchange interactions are equivalent on each honeycomb lattice bond. In parallel, the effects of exchange anisotropy on the spin frustration have also been explored to find possible QSLs and to understand their connection to the KSL [46–49]. They suggest that the strong z-bond region hosts large regions of disordered phases but it is not clear whether they correspond to the isolated dimer limit [47,48] or spin liquid states such as the Γ spin liquid (ΓSL) [30,43] or multinode gapless QSLs [49]. These numerical studies may also suffer from finite-size effects and thus an investigation of the classical $K\Gamma$ model whereby the bond strength is tuned would offer an insight to the ground states of the anisotropic $K\Gamma$ quantum model.

In this paper, we tackle this problem by addressing the following questions. What types of magnetic orderings appear

*hykee@physics.utoronto.ca

 ©2021 American Physical Society

via the competition between two extreme frustrated limits, i.e., Kitaev and Γ limits? How does the exchange anisotropy affect the classical ground states of the $K\Gamma$ model, and which regions of the anisotropic phase space may exhibit a quantum-disordered ground state? Using classical Monte Carlo simulations, we found various LUCs with intriguing fourfold or eightfold degeneracy except for a few special points with macroscopic degeneracy. It is likely that LUCs are results of the competition between the two frustrated Kitaev and Γ limits [38,44]. Near the Γ-dominant region, the bond strength anisotropy further enhances the quantum fluctuations leading to a complete destruction of the magnetic moment suggesting possible QSLs in this region.

The rest of the paper is organized as follows. In Sec. II we briefly discuss the physics of an isolated z bond before introducing x-and y-bond interactions, and then present the phase diagram of the two-dimensional model obtained via classical Monte Carlo simulations. In Sec. III we introduce three symmetry operations that map each bond Hamiltonian to itself, which reveals the degeneracy of each ordered phase independent of the bond anisotropy. In Sec. IV we focus on the phases near the Γ-dominant region, which arise from freezing the Ising degrees of freedom that form the classical ΓSL. In Sec. V we discuss the effects of quantum fluctuations using linear spin wave theory (LSWT) [50]. We then summarize our results and discuss implications of our findings on the quantum model in the last section.

II. DIMER HAMILTONIAN AND CLASSICAL PHASE DIAGRAM

We study the $K\Gamma$ model on the honeycomb lattice with bond anisotropy, where the Hamiltonian is given by

$$H = \sum_{\langle ij\rangle_\gamma} K^\gamma S_i^\gamma S_j^\gamma + \Gamma^\gamma \left(S_i^\alpha S_j^\beta + S_i^\beta S_j^\alpha\right), \tag{1}$$

where $\gamma \in \{x, y, z\}$, $\alpha, \beta \in \{x, y, z\}\backslash\gamma$ label the interaction along a particular bond. Here the spin direction $\vec{S}_i$ is defined in the local octahedral xyz basis as shown in Fig. 1. The crystallographic XYZ basis is also shown, where $\hat{Z} = \frac{1}{\sqrt{3}}(1, 1, 1)$ is perpendicular to the honeycomb plane, and $\hat{X} = \frac{1}{\sqrt{6}}(1, 1, -2)$, $\hat{Y} = \frac{1}{\sqrt{2}}(-1, 1, 0)$ are perpendicular and parallel to the z bonds, respectively. These will be used when we describe the magnetic ordering moment directions in Sec. III. $\bar{A}, \bar{B}, \bar{C}$ denoted by varying shades of gray in Fig. 1 represent the three $\sqrt{3}\times\sqrt{3}$ plaquette sublattices used in Secs. III and IV. The bond anisotropy is tuned by a parameter $g \in [0, 1]$ by introducing the interaction strengths as

$$\begin{aligned} K^{xy} &= -(1-g^2)K, \quad K^z = -K, \\ \Gamma^{xy} &= +(1-g^2)\Gamma, \quad \Gamma^z = +\Gamma, \end{aligned} \tag{2}$$

where $K = \cos\psi$ and $\Gamma = \sin\psi$ and $\psi \in [0, 0.5\pi]$ is chosen to study the region between the FM Kitaev limit ($\psi = 0$) and the AFM Γ limit ($\psi = \pi/2$).

The $g = 1$ limit corresponds to the case of isolated z bonds, whereas the three bonds are equivalent at the isotropic limit $g = 0$. We study the $\Gamma/K - g$ phase diagram using classical Monte Carlo to identify possible magnetic orderings, their origins, and competitions. Before we present the phase diagram, we analyze the dimer limit $g = 1$, which will be useful to understand several ordered phases appearing when $g \neq 1$. At $g = 1$ the $K\Gamma$ Hamiltonian is a sum of isolated z bonds denoted in red in Fig. 1, and for the $\langle 12\rangle_z$ bond it is given by

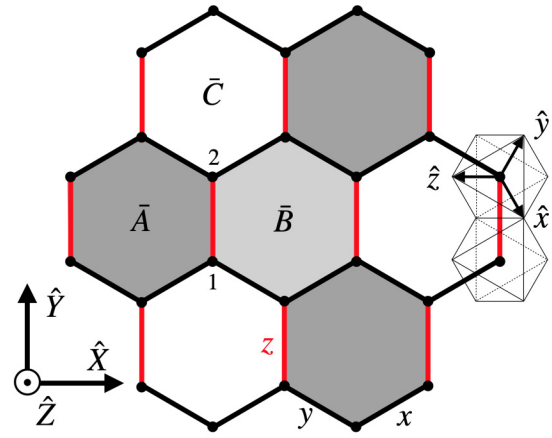

FIG. 1. The honeycomb lattice in the strong z-bond limit ($g > 0$) where the enhanced z-bond interaction strength is indicated in red and the xy chain extends horizontally. The three plaquette sublattices $\bar{A}, \bar{B}, \bar{C}$ are highlighted in dark gray, light gray, and white, respectively. The cubic xyz and crystallographic XYZ bases are also shown, where $\hat{Z}$ is perpendicular to the honeycomb plane and $\hat{X}, \hat{Y}$ are perpendicular and parallel to the z-bond direction, respectively.

$$H_{\langle 12\rangle_z} = K^z S_1^z S_2^z + \Gamma^z \left(S_1^x S_2^y + S_1^y S_2^x\right). \tag{3}$$

In the classical limit $\vec{S}_i$ can be parameterized by $S(\cos\phi_i \sin\theta_i, \sin\phi_i \sin\theta_i, \cos\theta_i)$ where $\phi_i \in [0, 2\pi)$ is the azimuthal angle in the xy plane and $\theta_i \in [0, \pi]$ is the polar angle from the z axis as in Fig. 1. The bond energy is minimized when $\theta_0 = \theta_1$ and $\phi_1 + \phi_2 = -\pi/2$ and the moments can be written as $\vec{S}_1 = S(a, b, c)$, $\vec{S}_2 = S(-b, -a, c)$ where $a, b, c \in \mathbb{R}$ satisfy $a^2 + b^2 + c^2 = 1$. The bond energy for this configuration is then

$$E_{\langle 12\rangle_z}/S^2 = -\Gamma - (K - \Gamma)c^2. \tag{4}$$

Note that when $K = \Gamma$ ($\psi = \pi/4$) each of the $N/2$ isolated z bonds retain an $O(3)$ symmetry, where N is the number of sites. Away from this point the $O(3)$ symmetry is lifted and one of two states may stabilize, while the macroscopic degeneracy associated with each z bond remains. When $K > \Gamma$ the energy is minimized by setting $c = 1$ and the moments form FM dimers pinned along the $\hat{z}$ direction with a twofold Ising degeneracy. On the other hand, when $\Gamma > K$ the bond energy is minimized by placing the moments in the xy plane. In this case the moments retain a continuous $O(2)$ degeneracy with the restriction that $\phi_1 + \phi_2 = -\pi/2$. The transition between the two phases is thus a first-order spin-flop transition. Introducing interactions along the x and y bonds when $g \neq 1$ may lift the macroscopic degeneracy and one may wonder what possible orderings arise from the peculiar point, and how far they can be extended, i.e., if they can survive all the way to the two-dimensional isotropic limit. To answer these questions, we solve the classical model numerically using simulated annealing Monte Carlo (SAMC) [51–53] on clusters of up to

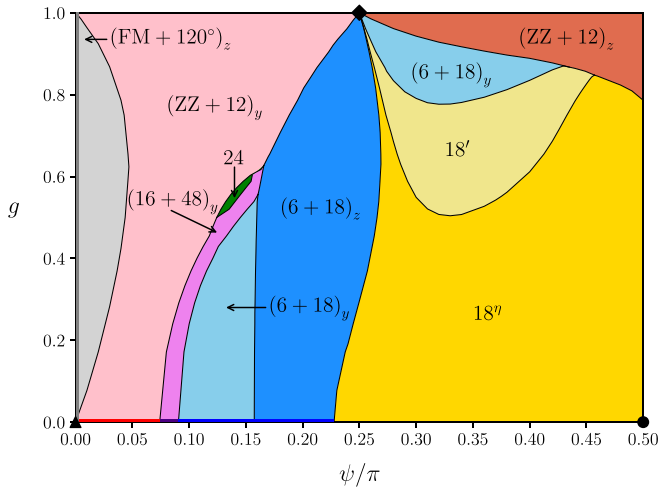

FIG. 2. The classical phase diagram of the anisotropic $K\Gamma$ model. All phases are separated by first-order transitions except for the 18^η and $18'$ phase boundary, which is of second-order. We highlight three points with macroscopic degeneracy, the $K=\Gamma$ dimer point and the pure isotropic K and Γ points, with a black diamond, triangle, and circle, respectively. In the isotropic limit the three orientations of $\mathrm{ZZ}+12$, $6+18$, and $16+48$ phases are degenerate, which we indicate by the dark red, dark blue, and dark purple lines along $g=0$, respectively. This degeneracy is lifted for $g\neq 0$ due to the broken C_3 symmetry. At $\psi=0$ we indicate the Kitaev FM dimer phase in dark gray, which immediately forms the $\mathrm{FM}+120°$ order in the presence of $\Gamma>0$. See the main text for the ordering patterns of the phases and their SSF peaks in Appendix B.

$N=720$ sites with $N\times 10^5$ MC steps, see Appendix A for simulation details.

We present the phase diagram in Fig. 2. The phase boundaries are obtained by comparing the energies of the classical states, and the nature of the phase transitions across the boundaries is determined by the first singular derivative of the ground-state energy per site E_0/N. The presence of magnetic order can be identified by sharp features in the static structure factor (SSF) $s_{\mathbf{k}}=\sum_{ij}\vec{S}_i\cdot\vec{S}_j\,e^{i\mathbf{k}\cdot(\mathbf{r}_i-\mathbf{r}_j)}$ where i,j range over all sites of the cluster and $\mathbf{r}_i$ is the vector pointing to site i.

The phase diagram shows several spin orderings and in Appendix B we show the SSF of each order. Following Ref. [38] we use the notation of n_1+n_2, where "+" represents the degeneracy of two orderings and n_i denotes the number of sites in the phase's magnetic unit cell. Three exceptions are the FM, zigzag (ZZ), and 120° orders, which have two, four, and six sites in the magnetic unit cell, respectively. In Fig. 2 we find the presence of these three phases as well as the six- and 16-site orders: the former appears in Refs. [37,38,54] and is composed of alternating zigzag and stripy chains, see Fig. 4(a) in the next section. Interestingly, some of these phases are degenerate with an order containing a larger unit cell with 12, 18, and 48 sites. There also exists the 18^η, $18'$, and 24-site orders, which do not have a smaller ordering counterpart. We note briefly that the LUC orders generally contain dominant SSF peaks at multiple wave vectors within the 1st (crystal) Brillouin zone. In particular the 18^η and $18'$ orders have finite spectral weight at the three $\mathbf{Q}=\frac{2}{3}M$, $\frac{4}{3}M$ points of the crystal Brillouin zone, see Appendix B.

We distinguish the phases that share the same ordering pattern but with a different moment orientation using a subscript of $i=x,y,z$. For example, the ZZ_z and ZZ_y both have four sites in the magnetic unit cell, but the zigzag chains repeat along the z-bond direction in the former and the y-bond direction in the latter. There is also a ZZ_x orientation that is degenerate with ZZ_y and can be obtained by a C_2 rotation about the z-bond direction $\hat{Y}$, but it is omitted in Fig. 2 for simplicity.

The pure classical Kitaev model exhibits an extensive ground-state degeneracy, and when $g>0$ the moments form disconnected FM dimers along the z bond, which point in the $\pm\hat{z}$ direction [34,35]. This is denoted by the solid gray line in Fig. 2. When Γ is turned on the magnetic order is stabilized and a FM is formed with moments pinned near the $\hat{z}$ axis. The 120° order, which is degenerate with the FM, can be obtained by a symmetry operation to be discussed in the next section. In a small region between the $(\mathrm{ZZ}+12)_y$ and $6+18$ regions we find $16+48$ and 24-site orders, which may arise from further moment frustration. Below we will focus our attention on the $\mathrm{ZZ}+12$, $6+18$, 18^η, and $18'$ phases, which occupy the majority of the phase space extending from the $K=\Gamma$ dimer point at $(\psi,g)=(0.25\pi,\,1)$ to the isotropic limit. The $\mathrm{ZZ}+12$ and $6+18$ orders are stabilized in the Kitaev-dominant region and are sensitive to anisotropy since a particular orientation is selected based on the values of g and Γ/K. On the other hand, the 18^η and $18'$ phases remain eightfold degenerate throughout their respective phase regions. In the next two sections we present the patterns of each magnetic order and the symmetries related to their degeneracy, and in Sec. V we will discuss the quantum effects on the magnetically ordered states using LSWT.

III. CLASSICAL $K\Gamma$ DEGENERATE MANIFOLDS

The degeneracy of the classical orders exhibited in Fig. 2 originates from a symmetry of the Hamiltonian Eq. (1). This can be seen by considering the dual honeycomb lattice, i.e., a triangular network with sites at the center of each hexagon labeled by the three plaquette sublattices $\bar{A}$, $\bar{B}$, $\bar{C}$ in Fig. 1. For a sublattice $\bar{\sigma}\in\{\bar{A},\,\bar{B},\,\bar{C}\}$, we define the operation

$$\mathcal{R}_{\bar{\sigma}}=\prod_{p\in\bar{\sigma}}\prod_{i\in\partial p}C_2^{\mathrm{out}(i)}, \tag{5}$$

where C_2^α is a π rotation about the cubic α axis and $\mathrm{out}(i)=x,y,z$ refers to the bond, which extends outwards from the plaquette $p\in\bar{\sigma}$ at site i. The notation ∂p refers to the boundary of the plaquette p, which consists of six bonds. For example, the $\langle 12\rangle_z$ bond Hamiltonian transforms under $\mathcal{R}_{\bar{A}}$ as

$$\begin{aligned}H_{\langle 12\rangle_z}&=K^z S_1^z S_2^z+\Gamma^z\left(S_1^xS_2^y+S_1^yS_2^x\right)\\&\xrightarrow{\mathcal{R}_{\bar{A}}}K^z\left(-S_1^z\right)\left(-S_2^z\right)+\Gamma^z\left[\left(-S_1^x\right)\left(-S_2^y\right)+S_1^yS_2^x\right]\\&=H_{\langle 12\rangle_z}.\end{aligned} \tag{6}$$

If we apply this operation to the remaining sites of the honeycomb lattice, the total Hamiltonian Eq. (1) maps to itself. This is the case for the $\mathcal{R}_{\bar{B}}$, $\mathcal{R}_{\bar{C}}$ operators defined for the plaquette sublattices $\bar{B}$, $\bar{C}$, respectively. Thus the Hamiltonian is intact under the three $\mathcal{R}_{\bar{\sigma}}$ symmetry operations of Eq. (5).

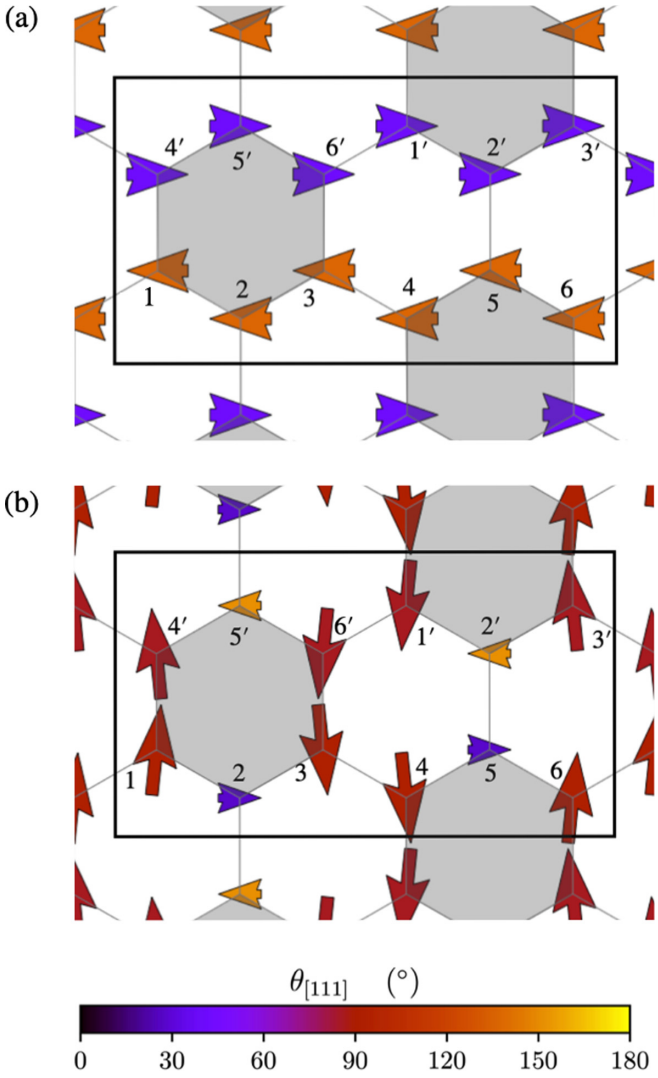

FIG. 3. The (a) ZZ_z and (b) 12_z configurations at $(\psi, g) = (0.4\pi, 0.94)$. The plaquette sublattice $\bar{A}$ is shown in gray. The color of each moment in Figs. 3–5 denotes the angle made with respect to the [111] direction.

Since $(\mathcal{R}_{\bar{\sigma}})^2 = \mathcal{R}_{\bar{A}}\mathcal{R}_{\bar{B}}\mathcal{R}_{\bar{C}} = 1$, the set $\{1, \mathcal{R}_{\bar{A}}, \mathcal{R}_{\bar{B}}, \mathcal{R}_{\bar{C}}\}$ is isomorphic to the Klein four-group $\mathbb{Z}_2 \times \mathbb{Z}_2$. This group leads to the degeneracy in all the phases shown in Fig. 2.

We note that the $\mathcal{R}_{\bar{\sigma}}$ transformations were first introduced in the context of the pure isotropic Γ model [40]. In this work we show that these operations continue to be symmetries of the $K\Gamma$ model with finite g.

Let us now explore the action of $\mathcal{R}_{\bar{\sigma}}$ on the phases shown in Fig. 2 using the $(ZZ + 12)_z$ orientation as an example. The ZZ_z orientation shown in Fig. 3(a) is given by FM chains of moments $\vec{S}_i = S(-a, -a, +c)$, $\vec{S}_{i'} = S(+a, +a, -c)$ separated by z bonds, where $|S^x_{i,i'}| = |S^y_{i,i'}| = S\,a$, $|S^z_{i,i'}| = S\,c$ and $2a^2 + c^2 = 1$. These moments lie in the crystallographic XZ plane and $a \gg c$ due to the proximity to the Γ dimer limit, which favors moments lying in the xy plane. Now we apply the symmetry operation $\mathcal{R}_{\bar{A}}$ on this configuration where $\bar{A}$ is the plaquette sublattice shown in dark gray in Fig. 3. Explicitly we perform C_2^x rotation on sites 1, 6, 1′, 6′, C_2^y on sites 3, 4, 3′, 4′, and C_2^z on sites 2, 5, 2′, 5′, which results in the 12-site order

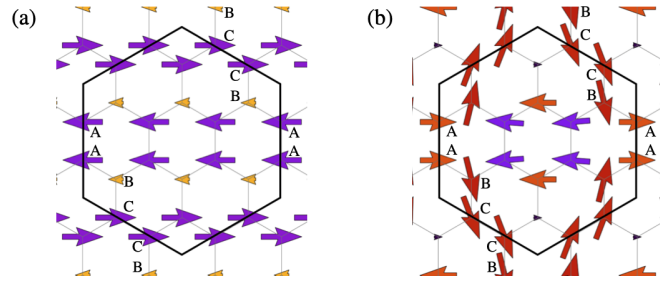

FIG. 4. The (a) 6_z and (b) 18_z configurations at $(\psi, g) = (0.25\pi, 0.84)$, where the counterrotating spiral pattern ABCCBA pattern is shown. Whereas the 6_z orientation contains a chain of FM aligned moments along the x and y bonds, in the 6_y orientation the chain runs along the x and z bonds.

shown in Fig. 3(b) given by

$$\begin{aligned}
\vec{S}_1 &= S(-a, +a, -c), & \vec{S}_{4'} &= S(-a, +a, +c),\\
\vec{S}_2 &= S(+a, +a, +c), & \vec{S}_{5'} &= S(-a, -a, -c),\\
\vec{S}_3 &= S(+a, -a, -c), & \vec{S}_{6'} &= S(+a, -a, +c),\\
\vec{S}_4 &= S(+a, -a, -c), & \vec{S}_{1'} &= S(+a, -a, +c),\\
\vec{S}_5 &= S(+a, +a, +c), & \vec{S}_{2'} &= S(-a, -a, -c),\\
\vec{S}_6 &= S(-a, +a, -c), & \vec{S}_{3'} &= S(-a, +a, +c). \qquad (7)
\end{aligned}$$

We call this particular orientation 12_z due to the two-site periodicity along the z bond as shown in Fig. 3(b). This shows that the two orders are degenerate. The two other operations $\mathcal{R}_{\bar{B},\bar{C}}$ applied on ZZ_z give the 12_z order up to translations of the magnetic unit cell, so that the total degeneracy due to $\mathcal{R}_{\bar{\sigma}}$ and time reversal $\mathcal{T} : \vec{S}_i \to -\vec{S}_i$ is four. Similarly, the $(ZZ + 12)_y$ orientation is fourfold degenerate but cannot be mapped to the $(ZZ + 12)_z$ orientations when $g \neq 0$ and a first-order transition separates the two. This analysis applies to the three orientations of the FM + 120°, 6 + 18, and 16 + 48 orders as well: the $(6 + 18)_z$ orientation is shown in Fig. 4.

From Eq. (7) we note that the moments in the 12_z configuration alternate in a six-site pattern ABCCBA along the xy chain. This is also the case for the 6 + 18 phases as indicated in Fig. 4. This pattern is referred to as a counterrotating spiral as the moments alternate as ABC along one site sublattice and ACB along the other, forming two FM dimers serving as inversion centers. This pattern has appeared in previous models of hyperhoneycomb materials [55–58] suggesting a relation between the 12 and 6 + 18 phases to the so-called K states of Ref. [57].

IV. FREEZING THE Γ SPIN LIQUID: 18^{η} AND $18'$ PHASES

In this section we focus on the 18^{η} and $18'$ phases, where there are four degenerate spin patterns (excluding time-reversal partners) with the same size of magnetic unit cell. One vortex pattern is denoted by 18^{η}_V (called 18-C_3 in Ref. [38]) and three patterns as 18^{η}_i for $i \in \{x, y, z\}$, see Fig. 5. Crucially, the four orientations are connected by the three $\mathcal{R}_{\bar{\sigma}}$ operations.

To discuss the appearance of the 18^{η} and $18'$ phases in the Γ-dominant limit, and the difference between the two,

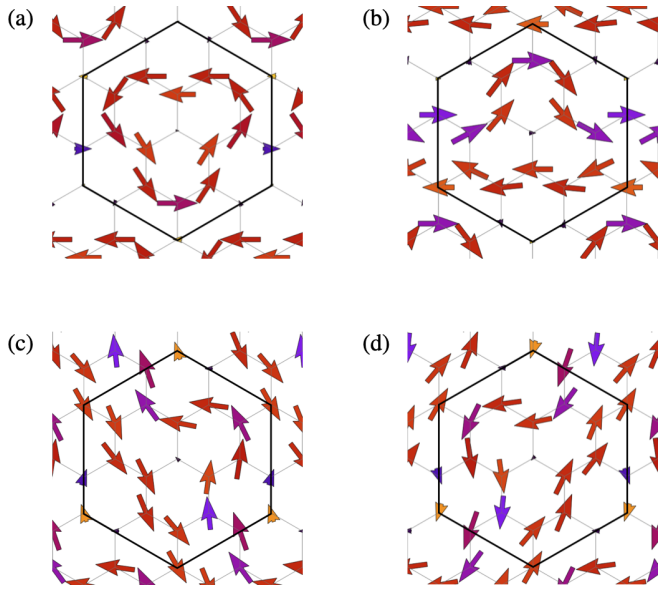

FIG. 5. The (a) 18^{η}_{V}, (b) 18^{η}_{z}, (c) 18^{η}_{x}, and (d) 18^{η}_{y} configurations at $(\psi,\ g) = (0.4\pi,\ 0.5)$.

we first review the physics of the isotropic Γ model. There it was found that the classical ground state is the Γ spin liquid (ΓSL), which contains an extensive degeneracy due to free Ising degrees of freedom $\eta_p = \pm 1$ that reside on each plaquette p in addition to a continuous $O(3)$ degeneracy [40]. This can be seen by separating the sign and magnitude of the spin components as

$$\vec{S}_i = \begin{cases} +S\left(\eta_i^x\, a_i,\ \eta_i^y\, b_i,\ \eta_i^z\, c_i\right) & i \in \text{A sublattice}, \\ -S\left(\eta_i^x\, a_i,\ \eta_i^y\, b_i,\ \eta_i^z\, c_i\right) & i \in \text{B sublattice}, \end{cases} \tag{8}$$

where A and B are the honeycomb site sublattices and $(a_i,\ b_i,\ c_i) = (|S_i^x|,\ |S_i^y|,\ |S_i^z|)/S$ satisfies $a_i^2 + b_i^2 + c_i^2 = 1$ and $\eta_i^\alpha = \pm 1, \alpha \in \{x,\ y,\ z\}$. We introduce a visual guide where each site i is represented by a triangle with each corner corresponding to one of the three η_i^α

$$\vec{\eta}_i = (\eta_i^x,\ \eta_i^y,\ \eta_i^z) = \begin{cases} \\ \\ \end{cases} \quad \begin{array}{l} i \in \text{A sublattice}, \\ \\ i \in \text{B sublattice}. \end{array} \tag{9}$$

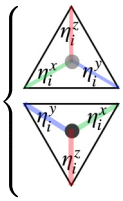

We refer to this as the η representation of the moments $\vec{S}_i$, which allows us to easily extract the role of the spin component signs η_i^α in the energy minimization process. For example the signs of the two energy contributions from Γ^z along the $\langle 12\rangle_z$ bond in Fig. 1 are $\text{sgn}(\Gamma^z S_1^x S_2^y) = -\eta_1^x \eta_2^y$ and $\text{sgn}(\Gamma^z S_1^y S_2^x) = -\eta_1^y \eta_2^x$, which are minimized for general a_i, b_i when $\eta_1^x \eta_2^y = \eta_1^y \eta_2^x = 1$. In the pure Γ limit all η constraints may be minimized by fixing the signs of an arbitrary site i as $(\eta_i^x,\ \eta_i^y,\ \eta_i^z) \equiv (\eta_1,\ \eta_2,\ \eta_3)$ and distributing the signs by satisfying the η constraints bond by bond, introducing new η's as necessary to parametrize the signs of any leftover spin components. One may see that each plaquette p may be assigned an Ising variable η_p by satisfying the η constraints along the

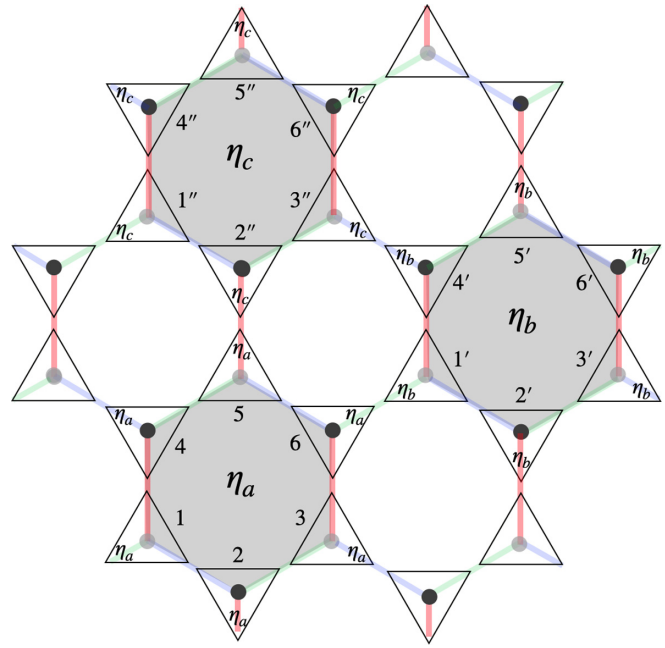

FIG. 6. η representation of the moments $\vec{S}_i$ in the pure Γ limit, where we only display the η_p that reside on the plaquette sublattice $\bar{A}$ (shown in gray) for clarity.

plaquette's boundary. Furthermore, the energy is insensitive to the value of η_p as each contribution squares to unity, so that the pure Γ limit is equivalent to an Ising gas on the triangular superlattice and exhibits an extensive ground-state degeneracy [40]. The combination of time reversal and one of the three global $\mathcal{R}_{\bar{\sigma}}$ transformations on the ΓSL corresponds to flipping the signs of all η_p which live on one of the plaquette sublattices $\bar{\sigma} \in \{\bar{A}, \bar{B}, \bar{C}\}$ [40,41]. For example, for the plaquettes shown in Fig. 6, applying $\mathcal{T} \cdot \mathcal{R}_{\bar{A}}$ on each moment gives

$$\begin{aligned} &\vec{S}_1 \to \left(-\eta_a |S_1^x|,\ S_1^y,\ S_1^z\right), \quad \vec{S}_4 \to \left(S_4^x,\ +\eta_a |S_4^y|,\ S_4^z\right), \\ &\vec{S}_2 \to \left(S_2^x,\ S_2^y,\ +\eta_a |S_2^z|\right), \quad \vec{S}_5 \to \left(S_5^x,\ S_5^y,\ -\eta_a |S_5^z|\right), \\ &\vec{S}_3 \to \left(S_3^x,\ -\eta_a |S_3^y|,\ S_3^z\right), \quad \vec{S}_6 \to \left(+\eta_a |S_6^x|,\ S_6^y,\ S_6^z\right), \end{aligned} \tag{10}$$

and similarly for the i' and i'' moments, which will flip the signs of η_b and η_c, respectively.

We add a finite Kitaev term and investigate the stability of the ΓSL. For the $\langle 61'\rangle_x$, $\langle 4'3''\rangle_y$, and $\langle 2''5\rangle_z$ bonds shown in Fig. 6, the Kitaev contributions to the energy come with sign

$$\begin{aligned} \text{sgn}\, E^K_{\langle 61'\rangle_x} &= -\text{sgn}\, K\, \eta_6^x\, \eta_{1'}^x = \eta_a\, \eta_b, \\ \text{sgn}\, E^K_{\langle 4'3''\rangle_y} &= -\text{sgn}\, K\, \eta_{4'}^y\, \eta_{3''}^y = \eta_b\, \eta_c, \\ \text{sgn}\, E^K_{\langle 2''5\rangle_z} &= -\text{sgn}\, K\, \eta_{2''}^z\, \eta_5^z = \eta_c\, \eta_a, \end{aligned} \tag{11}$$

and thus are minimized when $\eta_a\, \eta_b = \eta_b\, \eta_c = \eta_c\, \eta_a = -1$. The three $\eta_{a,b,c}$ cannot be fixed simultaneously without violating one of the η constraints, which shows that perturbing the ΓSL with Kitaev interactions is identical to the triangular Ising antiferromagnet with interactions between next-nearest-neighbor η variables [3,59,60]. It also presents a clear demonstration of the competition present between Kitaev and Γ interactions of opposite signs [44].

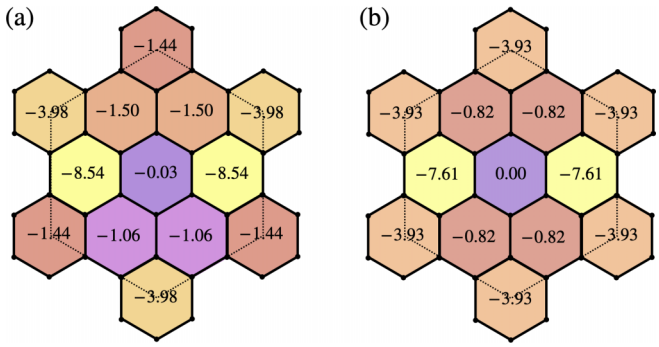

FIG. 7. The (a) 18^{η} order at $(\psi, g) = (0.4\pi, 0.5)$ and (b) $18'$ order at $(\psi, g) = (0.4\pi, 0.75)$, with the values of the plaquette flux W_p/S^6 shown in the center of each hexagon. The nine-plaquette unit cell is indicated by dashed lines. Note that in (b) the W_p are inversion symmetric about the zero-flux plaquette as the $18'$ phase respects inversion symmetry.

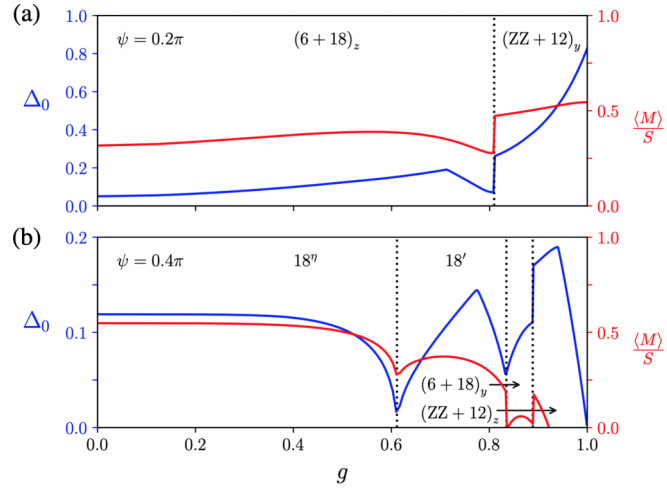

FIG. 8. Reduced moment $\langle M\rangle/S$ (red) and magnon gap Δ_0 (blue) as a function of g for (a) $\psi = 0.2\pi$ and (b) $\psi = 0.4\pi$. The classical phases stabilized in each region are labeled and the phase boundaries are indicated by the dashed black lines.

The ground state is obtained when two-thirds of all η_p carry one sign while the remaining third carry the opposite sign [3]. For next-nearest-neighbor interactions only, there are several configurations of η_p that minimize the energy [60]. However including the spin magnitude $|S_i^{\alpha}|$ lifts this degeneracy and selects the state with nine η_p, or 18 sites, in the magnetic unit cell. This is precisely the 18^{η} phase, which is a subset of the classical degenerate ground states of the ΓSL that is selected by FM K. Similar to the ΓSL the 18^{η} phase exhibits well-defined plaquette fluxes $W_p \equiv 2^6 \prod_{i\in\partial p} S_i^{\text{out}(i)} \neq 0$, see Fig. 7(a).

The $18'$ phase is separated from 18^{η} phase via a second-order transition. It is similar to the 18^{η} phase with eightfold degeneracy but the spin patterns respect inversion symmetry. We label the orientations of $18'_i$ as $i = x, y, z_1, z_2$ and we note that inversion maps each of $18'_{x,y}$ to itself, whereas $18'_{z_1}$ maps to $18'_{z_2}$ and vice versa. The $18'$ phase contains an idle plaquette with vanishing flux as shown in Fig. 7(b), and the six surrounding moments are pinned near the [100], [010], and [110] axes. Note that these moments lie in the xy plane, which reflects the increasing influence of the Γ dimer's $O(2)$ degeneracy discussed earlier as bond anisotropy is increased. Thus the 18^{η} and $18'$ phases result from the competing physics of the dimer and isotropic Γ limits in the presence of Kitaev interactions.

V. EFFECTS OF QUANTUM FLUCTUATIONS

In this section we discuss the effects of quantum fluctuations on the classical ground states by measuring the zero-point motion about the ordered state. Using LSWT the magnon gap is defined as $\Delta_0 = \min \omega^s_{\mathbf{k}} > 0$ where $\omega^s_{\mathbf{k}}$ are the magnon dispersions and s labels the sites of the magnetic unit cell. Increased quantum fluctuations lead to a reduction of the moment magnitude

$$\langle M\rangle = S - \frac{1}{N}\sum_i \langle a_i^{\dagger} a_i\rangle\,, \tag{12}$$

where $\langle a_i^{\dagger} a_i\rangle$ is the number of magnons per site in the ground state $|0\rangle$ at $T = 0$. In Fig. 8 we show two cuts where the bond anisotropy is varied at fixed Γ/K in the Kitaev-dominant limit $\psi = 0.2\pi\,(\Gamma/|K| \sim 0.73)$ and the Γ-dominant limit $\psi = 0.4\pi\,(\Gamma/|K| \sim 3.08)$. We indicate the magnon gap Δ_0 and the reduced moment $\langle M\rangle/S$ in blue and red, respectively. $\langle M\rangle/S \sim 0$ indicates that the classical order is unstable due to quantum fluctuations. Throughout both cuts the moment is reduced by more than 50% indicating strong quantum effects in all phases. However, the effects of anisotropy are qualitatively different between the K and Γ regimes. In the Kitaev-dominant region increased anisotropy leads to a decrease in moment reduction, and the gap increases due to the stability of the Ising easy axis at the pure dimer limit. On the other hand, in the Γ-dominant limit the gap goes to zero as anisotropy is increased. This is due to the proximity of the $O(2)$ symmetric Γ dimer, which exhibits gapless excitations within the xy plane as discussed in Sec. II. Interestingly, while the magnons are gapped away from this limit, the reduced moment indicates that quantum fluctuations become strong enough to completely destroy the magnetic order within LSWT.

The LSWT is valid up to $O(1/S)$ and can return an unphysical result when the number of magnons is large relative to S. This occurs in the presence of low-lying flat magnon bands where the magnon-magnon interactions cannot be ignored. In such a case the LSWT breaks down and accurate calculation of observables requires a proper accounting of effects beyond the single-magnon picture, which already tend to be significant in noncollinear magnetic orders [61–63]. Nevertheless the reduced moment provides a general estimate of the regions of the classical phase space which are most susceptible to a quantum-disordered state [64], and we find that such a phase may be stabilized in the Γ-dominant limit with moderate anisotropy.

VI. DISCUSSION AND SUMMARY

As we presented above, the $K\Gamma$ Hamiltonian with the bond anisotropy g is invariant under the $\mathcal{R}_{\bar{\sigma}}$ operators of

Eq. (5). However, when other interactions are present the symmetry is generally broken. This includes the first (J) and third (J_3) nearest-neighbor Heisenberg interactions and bond-dependent Γ' interactions, which are relevant for the description of Kitaev candidate materials [18,23,65]. For example, the J term on the $\langle 12\rangle_z$ bond in Fig. 1 transforms under $\mathcal{R}_{\bar{A}}$ as $J\vec{S}_1\cdot\vec{S}_2 \to J(-S_1^xS_2^x - S_1^yS_2^y + S_1^zS_2^z)$, and the Γ' term as $\Gamma'[S_1^xS_2^z + S_1^zS_2^x + (x\to y)] \to \Gamma'[S_1^xS_2^z - S_1^zS_2^x - (x\to y)]$. The external Zeeman field also breaks the symmetry. Thus the degeneracy related to this symmetry in all the magnetic orders shown in this study is lifted in the presence of any one or more of these terms. This explains several results of previous studies including how a FM Γ' lifts the $(\mathrm{ZZ}+12)_z$ degeneracy and selects the ZZ_z over the 12_z configurations [26,29,30,54,66]. Similarly the external magnetic field lifts the $\mathrm{ZZ}+12$ and $6+18$ degeneracies near the Kitaev region and selects the ZZ and six-site orders, respectively [38,67].

We compare our results with previous studies of the $K\Gamma$ model at the isotropic limit $g=0$. This was first explored in Ref. [9] where the classical limit shows the presence of an incommensurate spiral order along the $K\Gamma$ line using a single-**Q** variational ansatz. Further studies of the $K\Gamma$ line go beyond this approximation using classical Monte Carlo techniques [37–39,44,45]. More recently it was found that the incommensurate spiral order is stabilized at low temperatures $T\sim 0.1$–0.2 as exhibited by the magnetic susceptibility and heat capacity [39]. In contrast, we obtain the LUC orders in this region of $g=0$ when $T\sim 10^{-9}$ where thermal fluctuations are minuscule compared to the average interaction scale. We determine the energy of each phase to a high precision using the algorithm given in Ref. [38], i.e., by annealing the cluster to this ultralow temperature and then performing sweeps of the cluster where the moments are aligned with their local molecular fields, see Appendix A for details.

Numerical studies of the quantum model in the isotropic limit $g=0$ report various quantum-disordered phases including a proximate KSL (PKSL) [27,31,49], a ΓSL [30,43], and a nematic paramagnet [28,29]. Away from $g=0$, a disordered region between the isotropic limit and the dimer phase, which rapidly expands when $\Gamma > K$, was also reported [48]. However, it is not clear whether this is a true phase boundary or simply a crossover region connecting the two phases. A series of multinode gapless QSLs before entering a dimer phase at larger g was found using variational MC (VMC) [49]. A further VMC simulation including the multi-**Q** orders around the Γ region with finite g (i.e., 18^{η} and $18'$) would extend our current knowledge on possible QSLs and their nature in this region.

Here, for the classical $K\Gamma$ model with $g=0$ we find four different phases ($\mathrm{ZZ}+12$, $6+18$, $16+48$ and 18^{η}) with LUCs, and the LSWT shows that, in the Γ-dominant regime, the reduced moment $\langle M\rangle/S$ for fixed Γ/K in Fig. 8(b) decreases as g increases. This supports the disordered phases reported in Refs. [48,49]. Furthermore if the magnetic ordering in the $18^{\eta}_{x,y,z}$ orientations are destroyed by quantum fluctuations but the spontaneous C_3 symmetry breaking survives at $g=0$, it generates a nematic paramagnetic state. We emphasize though this broken lattice-rotational symmetry does not exclude a QSL.

Finally, an interesting proposal is a possible vison crystal spin liquid near the ΓSL. In fact, one feature of the ΓSL is significant correlations of the plaquette fluxes, which peak at the Γ and K, K' points in the reciprocal space [42,43]. A vison crystal spin liquid, which is magnetically disordered yet exhibits a broken translational symmetry in the form of a long-range $\langle W_pW_{p'}\rangle$ correlation function, may be stabilized in the Γ-dominant region with moderate z-bond anisotropy, which remains as a subject for future study.

In summary, we have studied the classical $K\Gamma$-g model to understand the phases out of two competing frustrated interactions and the effects of bond anisotropy on their competition. The pure Kitaev and Γ models have classical spin liquids with macroscopic degeneracy, but when they are both present, we found there exist several LUC phases occurring via their competition. All the phases have the intrinsic degeneracy related to a product of π rotations around the plaquette, where a subset of degenerate states can have a smaller magnetic unit cell as a special case of a larger magnetic unit cell state. Near the Γ-dominant region, we find 18-site magnetic unit cells, which retain their degeneracy in the presence of bond anisotropy unlike the C_3 related degeneracy appearing in the Kitaev-dominant region at $g=0$. The bond anisotropy enhances quantum fluctuations in the Γ-dominant region, which suggests that this region hosts a potential QSL.

ACKNOWLEDGMENTS

We would like to thank K. Chen, P. P. Stavropoulos, E. Z. Zhang, and J. Zhao for useful discussions. We acknowledge support from the NSERC Discovery Grant No. 06089-2016. H.-Y.K. also acknowledges support from CIFAR and the Canada Research Chairs Program. Computations were performed on the Niagara supercomputer at the SciNet HPC Consortium. SciNet is funded by the Canada Foundation for Innovation under the auspices of Compute Canada; the Government of Ontario, Ontario Research Fund–Research Excellence, and the University of Toronto.

APPENDIX A: MONTE CARLO SIMULATION DETAILS

We perform the SAMC simulation on a finite-size honeycomb cluster with periodic boundary conditions. We parametrize the honeycomb sites by placing them into unit cells located at $\mathbf{R}=\sum_i m_i\mathbf{T}_i$, where $\mathbf{T}_1$, $\mathbf{T}_2$ define the unit cell vectors and m_1, m_2 are integers. The honeycomb lattice contains $s\geqslant 2$ sublattices within a unit cell, each forming its own sublattice: every site i can be labeled by three integers $i=(m_1, m_2, t)$ where $t=1,\ldots,s$. One choice for the geometry of the unit cell is to use the two-site rhombic unit cell with translation vectors

$$\mathbf{T}_1=\mathbf{a}_1-\mathbf{a}_2=(1,\,0),$$
$$\mathbf{T}_2=\mathbf{a}_1=\left(\frac{1}{2},\,\frac{\sqrt{3}}{2}\right) \tag{A1}$$

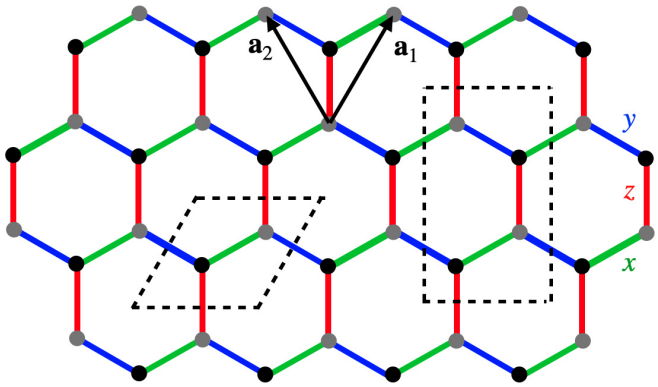

FIG. 9. The two unit cells used to construct the Monte Carlo cluster, with vectors $\mathbf{a}_1$ and $\mathbf{a}_2$ shown along with the three bond types. From left to right: the rhombic unit cell with unit cell vectors Eq. (A1) and the rectangular unit cell with unit cell vectors Eq. (A2). The bond type x, y, z are colored green, blue, and red, respectively.

which is shown in Fig. 9 along with $\mathbf{a}_{1,2}$. This choice produces a cluster that is commensurate with the 18 site phases when m_1 and m_2 are multiples of 3. We may also use the 4-site rectangular unit cell with translation vectors

$$\mathbf{T}_1 = \mathbf{a}_1 - \mathbf{a}_2 = (1,\ 0),$$
$$\mathbf{T}_2 = \mathbf{a}_1 + \mathbf{a}_2 = \left(0,\ \sqrt{3}\right), \tag{A2}$$

which produces a cluster commensurate with the $(\mathrm{ZZ}+12)_z$ order whenever m_1 is a multiple of 3. Either unit cell may be used to build the cluster as long as one ensures that the ordering wave vectors of the classical states are accessible. For our purposes we use the $N = 288$ site cluster with a

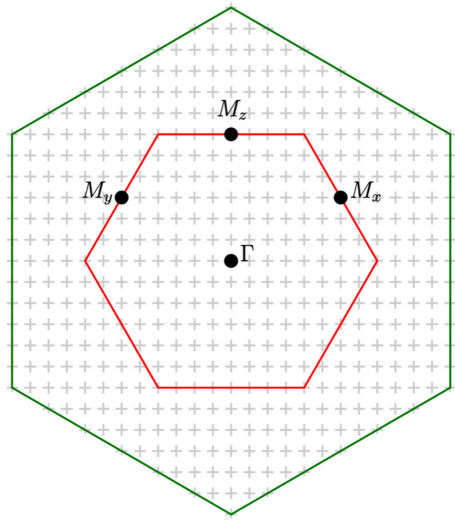

FIG. 10. The accessible momentum points for the $N = 4\times12\times6 = 288$ site cluster constructed using the rectangular unit cell in Eq. (A2). The red and green hexagons correspond to the first and second Brillouin zones, respectively. The three M points are shown and we use the label x, y, z to distinguish different orientations of the same magnetic order: see Appendix B.

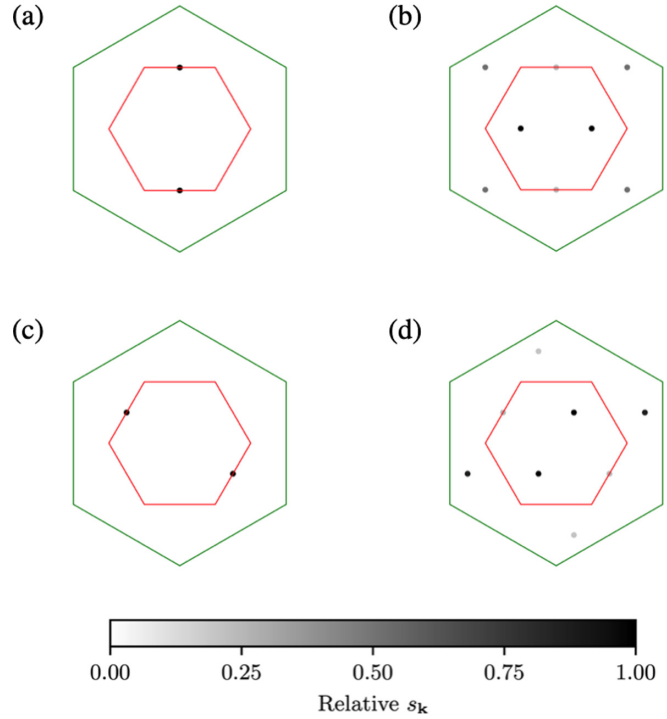

FIG. 11. SSF of the (a) ZZ_z and (b) 12_z patterns at $(\psi, g) = (0.4\pi, 0.94)$, as well as the (c) ZZ_y and (d) 12_y patterns at $(0.15\pi, 0.94)$ and $(0.1\pi, 0.65)$, respectively. The ZZ peaks are located at one of the three M points, whereas the 12-site peaks are located at one of three $\frac{1}{2}K$, $\frac{1}{2}K'$ pairs. The color of each ordering wave vector in Figs. 11–16 denotes the relative intensity of each peak.

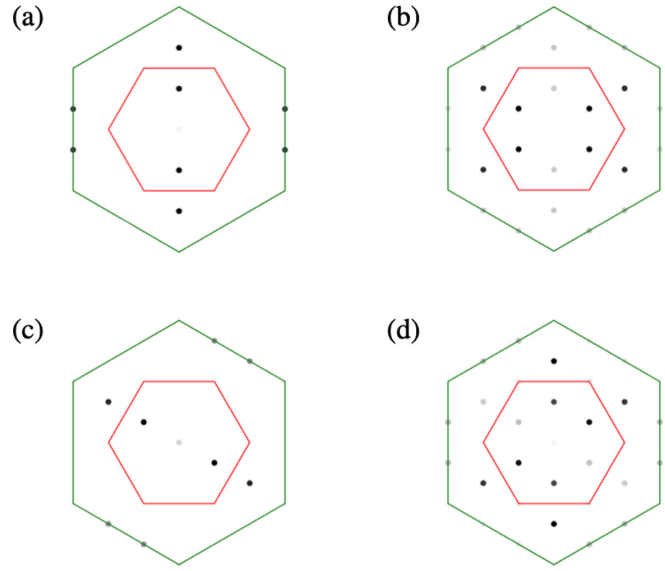

FIG. 12. SSF of the (a) 6_z and (b) 18_z patterns at $(0.25\pi, 0.84)$, as well as the (c) 6_y and (d) 18_y patterns at $(0.35\pi, 0.84)$. The six-site peaks are located at one of three $\frac{2}{3}M$, $\frac{4}{3}M$ pairs, whereas the 18-site peaks are located at multiple $\frac{2}{3}M$, $\frac{4}{3}M$ pairs.

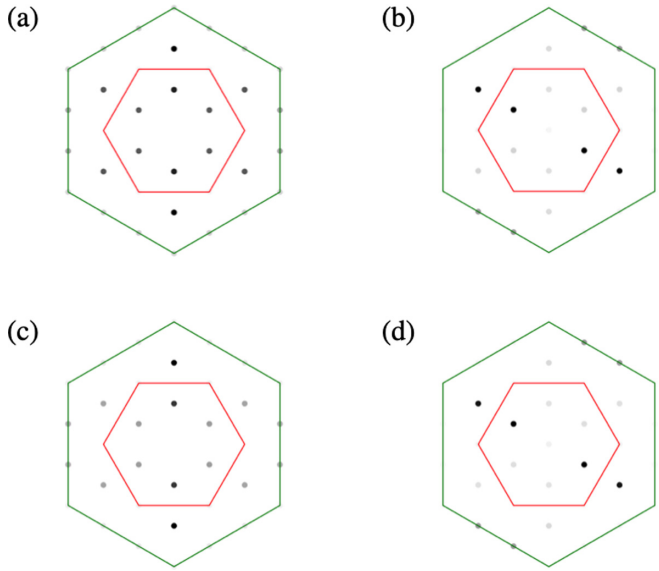

FIG. 13. SSF of the (a) 18^{η}_{V} and (b) 18^{η}_{y} patterns at $(0.4\pi, 0.5)$, as well as the (c) $18'_{z_1}$ and (d) $18'_{y}$ phase at $(0.4\pi, 0.71)$. The ordering vectors are located at multiple $\frac{2}{3}M$, $\frac{4}{3}M$ pairs.

rectangular unit cell, which accesses the M, $K/2$, and $2M/3$ reciprocal points as shown in Fig. 10. We have also extended the cluster size to $N = 720$ to check whether other large unit cell orders are stabilized.

After constructing the cluster we obtain the classical ground state using the SAMC algorithm given in Ref. [38], where Monte Carlo trials are performed for a finite temperature T, which is slowly tuned to zero. For our simulations we anneal according to the cooling schedule $T_{i+1} = 0.9\,T_i$ until the final temperature $T_f = (0.9)^{200} \sim 10^{-9}$ is reached. At each temperature step T_i of the simulation, we perform $N \times 10^5$ Metropolis trials where we choose a random moment, flip it so that it points in a random direction, and accept the new configuration with probability $\min(1, e^{-\Delta E/T})$ where ΔE is the energy difference between the two states. When the final temperature is reached, we further refine the energy by choosing a random moment and aligning it with its local molecular field, and then repeating this $N \times 10^4$ times.

In order to obtain the phase diagram Fig. 2 we first perform the SAMC on large clusters to resolve the possible classical ground states, and then refine the energy of each phase by

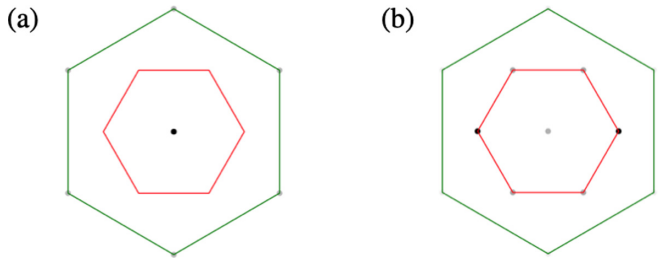

FIG. 14. SSF of the (a) FM_z and (b) 120°_z phase at $(0.04\pi, 0.5)$. The dominant SSF peak is at the Γ point for the FM phase and one of three K, K' pairs for the 120° phase.

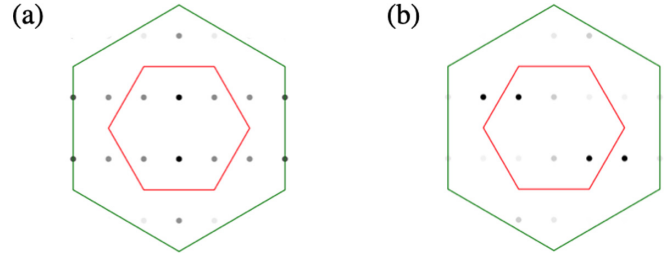

FIG. 15. SSF of the (a) 24_z and (b) 24_y patterns at $(0.125\pi, 0.57)$. The 24_z dominant SSF peaks are at $\frac{1}{2}M_z$ whereas for 24_y they are at $(\frac{1}{12}, \frac{5}{12})$, $(-\frac{1}{12}, \frac{7}{12})$ in the $\{\mathbf{b}_1, \mathbf{b}_2\}$ basis, where $\mathbf{b}_{1,2}$ satisfy $\mathbf{a}_i \cdot \mathbf{b}_j = 2\pi\delta_{ij}$.

either running the SAMC on small clusters or parametrizing the moments with angles (ϕ_i, θ_i) and minimizing the total energy within the unit cell with respect to each angle. To accurately obtain the $T = 0$ classical phase diagram it is important to determine each order's energy to full precision as the energy difference of the competing phases is within $\Delta E \sim O(10^{-3})$. Otherwise at higher temperatures one may stabilize a mixture of the competing phases. For example, the ZZ, six-site, and 16-site phases, which have SSF peaks along the Γ-M lines in reciprocal space, are close in energy for $\psi/\pi \sim 0.07$–0.09 along $g = 0$. A mixture of the three phases would appear as an incommensurate order with SSF peaks that vary along Γ-M, but such a state remains higher in energy than the true classical ground state at $T = 0$.

APPENDIX B: MAGNETIC ORDER OF THE $K\Gamma$ CLASSICAL GROUND STATES

We present in Figs. 11–16 the SSF patterns of the phases shown in the phase diagram Fig. 2. In each plot we show the first and second Brillouin zones in red and green, respectively. Different orderings, which share the same size of magnetic unit cell but with different moment orientations, are distinguished by a subscript $i = x, y, z$. These labels are assigned by the distribution of the SSF ordering vectors about one of the three Γ-M_i lines in Fig. 10.

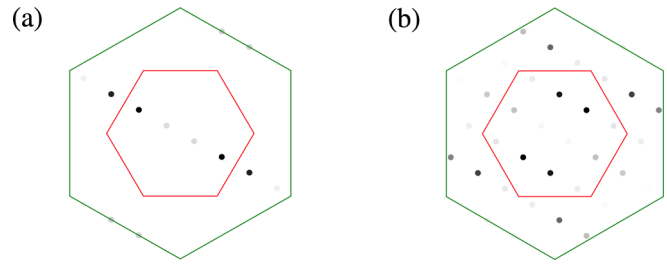

FIG. 16. SSF of the (a) 16_y and (b) 48_y patterns at $(0.14\pi, 0.5)$. The 16_y dominant SSF peaks are at $\frac{3}{4}M_y$, $\frac{5}{4}M_y$, whereas for 48_y they are at $(-\frac{1}{3}, -\frac{1}{24})$, $(\frac{1}{3}, \frac{7}{24})$ in the $\{\mathbf{b}_1, \mathbf{b}_2\}$ basis, where $\mathbf{b}_{1,2}$ satisfy $\mathbf{a}_i \cdot \mathbf{b}_j = 2\pi\delta_{ij}$.

[1] A. Kitaev, Ann. Phys. (NY) **321**, 2 (2006).
[2] A. Y. Kitaev, Ann. Phys. (NY) **303**, 2 (2003).
[3] G. H. Wannier, Phys. Rev. **79**, 357 (1950).
[4] P. W. Anderson, Mater. Res. Bull. **8**, 153 (1973).
[5] P. W. Anderson, Science **235**, 1196 (1987).
[6] L. Balents, Nature (London) **464**, 199 (2010).
[7] G. Jackeli and G. Khaliullin, Phys. Rev. Lett. **102**, 017205 (2009).
[8] J. Chaloupka, G. Jackeli, and G. Khaliullin, Phys. Rev. Lett. **105**, 027204 (2010).
[9] J. G. Rau, E. K.-H. Lee, and H.-Y. Kee, Phys. Rev. Lett. **112**, 077204 (2014).
[10] K. W. Plumb, J. P. Clancy, L. J. Sandilands, V. Shankar Venkataraman, Y. F. Hu, K. S. Burch, H.-Y. Kee, and Y.-J. Kim, Phys. Rev. B **90**, 041112(R) (2014).
[11] H.-S. Kim, V. Shankar Venkataraman, A. Catuneanu, and H.-Y. Kee, Phys. Rev. B **91**, 241110(R) (2015).
[12] A. Koitzsch, C. Habenicht, E. Müller, M. Knupfer, B. Büchner, H. C. Kandpal, J. van den Brink, D. Nowak, A. Isaeva, and T. Doert, Phys. Rev. Lett. **117**, 126403 (2016).
[13] L. J. Sandilands, Y. Tian, A. A. Reijnders, H.-S. Kim, K. W. Plumb, Y.-J. Kim, H.-Y. Kee, and K. S. Burch, Phys. Rev. B **93**, 075144 (2016).
[14] X. Zhou, H. Li, J. A. Waugh, S. Parham, H.-S. Kim, J. A. Sears, A. Gomes, H.-Y. Kee, Y.-J. Kim, and D. S. Dessau, Phys. Rev. B **94**, 161106(R) (2016).
[15] A. Banerjee, C. A. Bridges, J.Q. Yan, A. A. Aczel, L. Li, M. B. Stone, G. E. Granroth, M. D. Lumsden, Y. Yiu, J. Knolle *et al.*, Nat. Mater. **15**, 733 (2016).
[16] H.-S. Kim and H.-Y. Kee, Phys. Rev. B **93**, 155143 (2016).
[17] S. M. Winter, Y. Li, H. O. Jeschke, and R. Valentí, Phys. Rev. B **93**, 214431 (2016).
[18] J. G. Rau, E. K.-H. Lee, and H.-Y. Kee, Annu. Rev. Condens. Matter Phys. **7**, 195 (2016).
[19] L. Janssen, E. C. Andrade, and M. Vojta, Phys. Rev. B **96**, 064430 (2017).
[20] S. M. Winter, A. A. Tsirlin, M. Daghofer, J. van den Brink, Y. Singh, P. Gegenwart, and R. Valentí, J. Phys.: Condens. Matter **29**, 493002 (2017).
[21] W. Wang, Z.-Y. Dong, S.-L. Yu, and J.-X. Li, Phys. Rev. B **96**, 115103 (2017).
[22] M. Hermanns, I. Kimchi, and J. Knolle, Annu. Rev. Condens. Matter Phys. **9**, 17 (2018).
[23] H. Takagi, T. Takayama, G. Jackeli, G. Khaliullin, and S. E. Nagler, Nat. Rev. Phys. **1**, 264 (2019).
[24] P. Laurell and S. Okamoto, npj Quantum Mater. **5**, 2 (2020).
[25] M. Gohlke, G. Wachtel, Y. Yamaji, F. Pollmann, and Y. B. Kim, Phys. Rev. B **97**, 075126 (2018).
[26] J. S. Gordon, A. Catuneanu, E. S. Sørensen, and H.-Y. Kee, Nat. Commun. **10**, 2470 (2019).
[27] J. Wang, B. Normand, and Z.-X. Liu, Phys. Rev. Lett. **123**, 197201 (2019).
[28] M. Gohlke, L. E. Chern, H.-Y. Kee, and Y. B. Kim, Phys. Rev. Research **2**, 043023 (2020).
[29] H.-Y. Lee, R. Kaneko, L. E. Chern, T. Okubo, Y. Yamaji, N. Kawashima, and Y. B. Kim, Nat. Commun. **11**, 1639 (2020).
[30] Q. Luo, P. P. Stavropoulos, and H.-Y. Kee, arXiv:2010.11233.
[31] J. Wang, Q. Zhao, X. Wang, and Z.-X. Liu, Phys. Rev. B **102**, 144427 (2020).
[32] S.-S. Zhang, G. B. Halasz, W. Zhu, and C. D. Batista, Phys. Rev. B **104**, 014411 (2021).
[33] J. Rusnačko, D. Gotfryd, and J. Chaloupka, Phys. Rev. B **99**, 064425 (2019).
[34] G. Baskaran, D. Sen, and R. Shankar, Phys. Rev. B **78**, 115116 (2008).
[35] S. Chandra, K. Ramola, and D. Dhar, Phys. Rev. E **82**, 031113 (2010).
[36] I. Rousochatzakis, Y. Sizyuk, and N. B. Perkins, Nat. Commun. **9**, 1575 (2018).
[37] C. Balz, L. Janssen, P. Lampen-Kelley, A. Banerjee, Y. H. Liu, J. Q. Yan, D. G. Mandrus, M. Vojta, and S. E. Nagler, Phys. Rev. B **103**, 174417 (2021).
[38] L. E. Chern, R. Kaneko, H.-Y. Lee, and Y. B. Kim, Phys. Rev. Research **2**, 013014 (2020).
[39] M. Sun, H. Lin, Z. Zhang, Y. Cai, W. Ren, J. Kang, J. Ji, F. Jin, X. Wang, R. Yu, Q. Zhang, and Z. Liu, Chin. Phys. B **30**, 087503 (2021).
[40] I. Rousochatzakis and N. B. Perkins, Phys. Rev. Lett. **118**, 147204 (2017).
[41] A. M. Samarakoon, G. Wachtel, Y. Yamaji, D. A. Tennant, C. D. Batista, and Y. B. Kim, Phys. Rev. B **98**, 045121 (2018).
[42] P. Saha, Z. Fan, D. Zhang, and G.-W. Chern, Phys. Rev. Lett. **122**, 257204 (2019).
[43] Q. Luo, J. Zhao, H.-Y. Kee, and X. Wang, npj Quantum Mater. **6**, 57 (2021).
[44] K. Liu, N. Sadoune, N. Rao, J. Greitemann, and L. Pollet, Phys. Rev. Research **3**, 023016 (2021).
[45] N. Rao, K. Liu, M. Machaczek, and L. Pollet, Phys. Rev. Research **3**, 033223 (2021).
[46] A. Catuneanu, Y. Yamaji, G. Wachtel, Y. B. Kim, and H.-Y. Kee, npj Quantum Mater. **3**, 23 (2018).
[47] G. Wachtel and D. Orgad, Phys. Rev. B **99**, 115104 (2019).
[48] T. Yamada, T. Suzuki, and S. I. Suga, Phys. Rev. B **102**, 024415 (2020).
[49] J. Wang and Z.-X. Liu, Phys. Rev. B **102**, 094416 (2020).
[50] A. G. D. Maestro and M. J. P. Gingras, J. Phys.: Condens. Matter **16**, 3339 (2004).
[51] N. Metropolis, A. W. Rosenbluth, M. N. Rosenbluth, A. H. Teller, and E. Teller, J. Chem. Phys. **21**, 1087 (1953).
[52] S. Kirkpatrick, C. D. Gelatt, and M. P. Vecchi, Science **220**, 671 (1983).
[53] S. Kirkpatrick, J. Stat. Phys. **34**, 975 (1984).
[54] J. G. Rau and H.-Y. Kee, arXiv:1408.4811.
[55] E. K.-H. Lee and Y. B. Kim, Phys. Rev. B **91**, 064407 (2015).
[56] I. Kimchi and R. Coldea, Phys. Rev. B **94**, 201110(R) (2016).
[57] S. Ducatman, I. Rousochatzakis, and N. B. Perkins, Phys. Rev. B **97**, 125125 (2018).
[58] P. P. Stavropoulos, A. Catuneanu, and H.-Y. Kee, Phys. Rev. B **98**, 104401 (2018).
[59] Y. Tanaka and N. Uryû, J. Phys. Soc. Jpn. **39**, 825 (1975).
[60] U. Brandt and J. Stozle, Z. Phys. B: Condens. Matter **64**, 481 (1986).
[61] P. M. Consoli, L. Janssen, M. Vojta, and E. C. Andrade, Phys. Rev. B **102**, 155134 (2020).

[62] R. L. Smit, S. Keupert, O. Tsyplyatyev, P. A. Maksimov, A. L. Chernyshev, and P. Kopietz, Phys. Rev. B **101**, 054424 (2020).

[63] P. A. Maksimov and A. L. Chernyshev, Phys. Rev. Research **2**, 033011 (2020).

[64] P. Fazekas, *Lecture Notes on Electron Correlation and Magnetism* (World Scientific, Singapore, 1999).

[65] Y. Motome, R. Sano, S. Jang, Y. Sugita, and Y. Kato, J. Phys.: Condens. Matter **32**, 404001 (2020).

[66] K. Hwang, A. Go, J. H. Seong, T. Shibauchi, and E.-G. Moon, arXiv:2004.06119.

[67] E. Z. Zhang, L. E. Chern, and Y. B. Kim, Phys. Rev. B **103**, 174402 (2021).